Acta Materialia 115 (2016) 314–323

Contents lists available at ScienceDirect

Acta Materialia

journal homepage: www.elsevier.com/locate/actamat

Full length article

Quantification of dislocation structures from anelastic deformation behaviour

Zaloa Arechabaleta [a, *], Peter van Liempt [b], Jilt Sietsma [a]

[a] Department of Materials Science and Engineering, Delft University of Technology, Mekelweg 2, 2628 CD, Delft, The Netherlands
[b] Tata Steel Research, Development and Technology, Postbus 10000 (3G37), 1970 CA, IJmuiden, The Netherlands

ARTICLE INFO

Article history:
Received 18 March 2016
Received in revised form
24 May 2016
Accepted 25 May 2016
Available online 14 June 2016

Keywords:
Anelastic strain
Dislocation structure
Tensile test
X-ray diffraction

ABSTRACT

The pre-yield deformation behaviour (i.e., at stresses below the yield stress) of two materials, pure iron and a low-alloy steel, and its anelastic nature are analysed at room temperature, before and after the dislocation structures are varied by plastic deformation. It is shown, based on tensile experiments, that this behaviour can be explained by limited reversible glide of dislocations without essential changes in the dislocation structure. Moreover, a physically-based model that characterises the dislocation structure by two variables, the dislocation density and the effective dislocation segment length, is used to quantitatively describe this deformation behaviour. The model validity is further evaluated by comparison with dislocation densities from X-Ray Diffraction measurements.

1. Introduction

Sheet metal forming processes are extensively used in many sectors. Yet, the dimensional control of the formed sheets is a real challenge: springback -defined as the strain relaxation after release of the forming stresses- cannot be predicted accurately. Experimental evidence has shown that the magnitude of springback is not only dependent on the elastically recovered strain, but also on an anelastic contribution to the total relaxed strain [1–3]. The former, determined by the atomic interactions, is given by Hooke's law, whereas the latter is caused by dislocations within the material [1,4]. However, how do the dislocations cause this anelasticity? Already below the yield stress, dislocation segments bow out, causing an additional strain component, and thus the well-known reduction of the Young's modulus after plastic deformation [2,5,6]. This additional strain component is defined in this study as anelastic strain, according to [4,7], and is responsible for the non-linearity that is often observed in the stress-strain curve regime below the yield stress. If the load is released at any stage before the material starts to yield, this behaviour is reversible and the dislocations return to an equilibrium configuration. Once the yield stress is reached, Frank-Read sources are activated and the dislocations multiply. After plastic deformation and during unloading, the mobile dislocations move in the reverse direction, so similar mechanisms as those occurring in the pre-yield regime (with an increased dislocation density) are expected to reverse the anelastic strain, and lead to the springback phenomenon. Anelastic strain, as it is defined here, is related to the dislocations' subcritical bowing during loading and reversible bowing during unloading [8,9], which are essentially time independent at room temperature.

A better comprehension of the anelastic dislocation behaviour is essential for a complete physical model of the pre-yield behaviour of metals. Recently, a dislocation based model has been developed by van Liempt et al. [1] to account for the anelastic deformation in the pre-yield regime. The model, summarised in Section 2, quantifies the anelastic contribution as a function of two variables that characterise the dislocation structure in the material: the dislocation density and the effective dislocation segment length.

In this work, the pre-yield deformation behaviour of two materials, pure iron and a low-alloy steel, is analysed at room temperature using tensile tests. It is seen that this behaviour can be adequately explained by considering that, besides elastic strain, limited glide of dislocations does occur below the yield stress. The experimental results are discussed and quantified in relation with the predictions by the model for anelastic deformation. The model is validated by means of X-Ray Diffraction (XRD), by comparison of the dislocation density values obtained through the model

* Corresponding author.
E-mail addresses: z.arechabaletaguenechea@tudelft.nl (Z. Arechabaleta), peter.van-liempt@tatasteel.com (P. van Liempt), j.sietsma@tudelft.nl (J. Sietsma).

http://dx.doi.org/10.1016/j.actamat.2016.05.040
1359-6454/

application to the tensile curves with the values from the XRD analysis.

2. Anelastic behaviour of dislocations

During loading in the pre-yield regime, purely elastic strain due to atomic interactions, ε_e, and anelastic strain due to bowing-out of dislocation segments, ε_a, are simultaneously occurring, so the total strain ε_{pre} can be described as the sum of both contributions:

$$\varepsilon_{pre} = \varepsilon_e + \varepsilon_a = (\sigma/E) + \varepsilon_a \tag{1}$$

where σ is the applied stress and E is the elastic modulus of the crystal lattice. The stiffness in the pre-yield regime can be characterised by the derivative of the previous equation, which is:

$$\Theta_{pre} = \mathrm{d}\sigma/\mathrm{d}\varepsilon_{pre} = E\Theta_a/(E + \Theta_a) \tag{2}$$

where Θ_{pre} is the slope of the pre-yield stress-strain curve and $\Theta_a = \mathrm{d}\sigma/\mathrm{d}\varepsilon_a$ is the anelastic contribution to the pre-yield deformation behaviour. The latter is determined by the dislocation structure and behaviour. In order to analyse this behaviour, we consider a dislocation segment of length l pinned by other dislocation nodes, solute atoms or precipitates, as in Fig. 1(a). An applied shear stress τ causes the dislocation segment, initially at rest, to bow out and produce slip under the action of a glide force (Fig. 1(b)). This (limited) dislocation motion causes the anelastic strain. For N dislocation segments of length l per unit volume, the total anelastic shear strain γ_a can be expressed as:

$$\gamma_a = NbA \tag{3}$$

in which b is the length of the Burgers vector and A is the area swept by each dislocation. This area can be determined using the expression for a circle segment area:

$$A = \frac{1}{2}r^2(\varphi - \sin\varphi) \tag{4}$$

in which r is the radius of curvature and φ is the subtended angle (see Fig. 1(b)). In order to determine the anelastic contribution for any stress value within $0 < \sigma \leq \sigma_y$, the exact expression for the subtended angle φ is used:

$$\varphi = 2\arcsin(l/2r) \tag{5}$$

The only force that opposes the applied shear stress τ is the back stress due to the line tension of the dislocation, $T = Gb/2r$, where G is the shear modulus. For a small applied stress, the dislocation segment reaches an equilibrium position when $\tau = T$. The radius of curvature is then given by:

$$r = Gb/2\tau \tag{6}$$

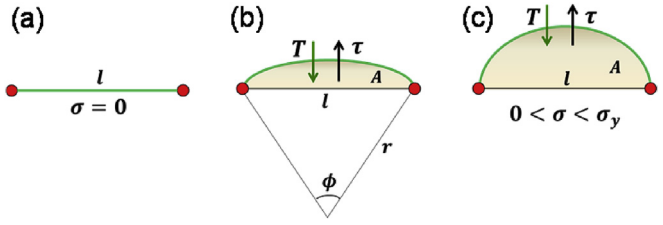

Fig. 1. Scheme of the bow-out mechanism of a dislocation below the yield stress. (a) The dislocation at an equilibrium configuration, (b) and (c) after bowing out to different curvatures.

As the shear stress τ increases, the area A swept by the dislocation and thus the anelastic strain γ_a increase. This process, as pointed out before, is reversible below the yield stress. At the yield stress, however, the radius of curvature r reaches its minimum ($r_{min} = l/2$) and the bowing-out becomes instable. Beyond this point, Equation (6) is no longer satisfied and dislocation loops start to form from the Frank-Read source. Plastic deformation has then begun. Consequently, the yield stress σ_y can be defined as the critical stress σ_c above which the bow-out mechanism is non-reversible. The yield stress σ_y can therefore be expressed by:

$$\sigma_y = \sigma_c = \overline{M}Gb/l \tag{7}$$

where $\overline{M}$ is the Taylor factor. Using Equations (3)–(7), the anelastic contribution can be determined in the entire pre-yield regime as follows [1]:

$$\Theta_a = \mathrm{d}\sigma/\mathrm{d}\varepsilon_a = \left[\overline{M}^2 Es^3\sqrt{(1-s^2)}\right] \Big/ \left[\rho l^2(1+\nu)\left(s - \sqrt{(1-s^2)}\arcsin s\right)\right] \tag{8}$$

where s is the stress normalised by the critical stress, $s = \sigma/\sigma_c$, ρ is the dislocation density and ν is Poisson's ratio. It must be noticed here that $Nl^3 = \rho l^2$. Finally, the pre-yield stiffness is obtained, substituting Equation (8) into Equation (2), as:

$$\Theta_{pre} = \frac{\overline{M}^2 Es^3\sqrt{(1-s^2)}}{\overline{M}^2 s^3\sqrt{(1-s^2)} + \rho l^2(1+\nu)\left(s - \sqrt{(1-s^2)}\arcsin s\right)} \tag{9}$$

It should be noted that the lengths of dislocation segments in a real material will form a distribution, which will cause the yield stress not to be a single value. The parameter l in the model description should be regarded as an effective value related to the effective average yield stress. Longer segments will be activated as Frank-Read sources at somewhat lower stress, shorter segments at higher stress. The extension of the yield-stress range is directly related to the width of the segment-length distribution. A wider segment-length distribution will cause a more gradual transition between the pre-yield and post-yield ranges in the extended Kocks-Mecking plot (see Section 4.1).

3. Experimental procedure

3.1. Materials

Two materials, with chemical compositions listed in Table 1, were selected for this study: pure iron (ARMCO pure iron, cold rolled and subsequently annealed, provided by AK Steel International) and a low-alloy steel (99.5% iron foil, as-rolled, provided by Goodfellow Cambridge Ltd.). The microstructure of the as-received materials was characterised by optical microscopy and the grain size was measured according to the equivalent diameter procedure. Fig. 2 shows the ferritic microstructures, which were revealed using a 2%Nital solution, together with the grain size measured in each case. The rolling and transverse directions (designated as RD and TD, respectively) are indicated. From the micrographs, it can be noticed that the pure iron exhibits a larger grain size than the steel, that is, 27 vs. 11 μm. Additional analysis revealed that there is no significant texture, and consequently, grains can be considered randomly oriented for both materials.

Table 1
Chemical composition (wt.%) of the materials selected for this study.

Material	C	Mn	P	S	N	Si	Al	Ni	Cr
Pure Fe	0.003	0.050	0.005	0.003	0.0051	0.004	0.003	0.015	0.017
Steel	<0.08	0.3	<0.04	<0.05		0.1			

3.2. Mechanical tests

Monotonic tensile tests were conducted on an Instron 5500R electromechanical tester, equipped with a load cell of 10 kN capacity, at room temperature and in displacement control. The tensile specimens were rectangular of dimensions 90 × 10 × 2 mm^3 and 90 × 10 × 1 mm^3 for the pure iron and the steel, respectively. The axial directions of the samples were aligned with the rolling direction of the sheets. Experimental evidence has shown that the derivative of the stress-strain curve (also known as the Kocks-Mecking plot [10]) is very sensitive to sample bending and/or incorrect alignment effects, despite these being small. In order to avoid these effects, two knife-edge type extensometers (Instron 2620 – 602, 12.5 mm gauge length, ±2.5 mm and an accuracy of ±0.5% of the read value) were placed on either side of the specimen and the average strain was used for the calculations. The crosshead speed was maintained constant at 1 mm/min, which is equivalent to a strain rate of the order of 10^{-5} s^{-1} in the pre-yield regime. At this strain rate, resistance effects due to thermally activated dislocation glide (i.e., lattice friction) can be considered negligible [11].

Each specimen was subjected to a double loading procedure, consisting of the following stages (in all of them, the crosshead speed was maintained at 1 mm/min):

(I) Loading in the pre-yield regime.
(II) Plastic deformation up to 14% strain for the pure iron and 15% strain for the low-alloy steel.
(III) Unloading.
(IV) Re-loading in the pre-yield regime.
(V) Plastic deformation by an additional 3%.
(VI) Unloading.

The stages (I) and (IV) were used to analyse the dislocation structure according to the model presented in Section 2 and reference [1]. XRD measurements were performed before stage (I) and after stage (III). For each material, three samples were tested to check the reproducibility of the results and the dispersion in the measurements.

Additionally, a different type of experiment was carried out for the low-alloy steel in order to investigate the strain reversibility in the pre-yield regime. This test was performed using the same conditions as in the monotonic tensile tests and involved a loading-unloading cycle below the yield stress after 3% plastic deformation. The maximum stress in this cycle was 266 MPa and the minimum stress was slightly above zero.

3.3. X-Ray Diffraction (XRD) measurements

The XRD measurements were conducted on a Bruker D8-Advance diffractometer operating at 45 kV and 30 mA, using Cu Kα radiation (λ = 0.15406 nm) and a scan rate of 0.002 s^{-1}. The diffraction profiles of the ferrite (110), (200), (211), (220), (310) and (222) reflections measured for the pure iron and the steel in the as-received and deformed conditions, respectively, were separated into $K\alpha_1$ and $K\alpha_2$ contributions. Peaks corresponding to $K\alpha_2$ as well as the background were subtracted from the profiles [14]. In order to completely remove instrumental effects, the diffraction patterns of the as-received undeformed pure iron and steel were used as a reference. In this way, it is assured that the difference in peak broadening between the deformed and as-received conditions is strictly caused by dislocations. Two of these measurements were performed for each material. The dislocation density was calculated combining the modified Williamson-Hall and Warren-Averbach methods (hereafter mWH and mWA, respectively) [12–14], which are widely reported in the literature. For more details on the XRD analysis see Appendix A.

4. Results and discussion

4.1. The experimental pre-yield deformation behaviour

Fig. 3 shows the true stress-true strain curves obtained for the three samples of the pure iron and the steel tested in this work. The plots show the pre-yield loading parts of the tensile curves in detail, stage (I) and stage (IV), respectively, as well as the first unloading, stage (III). Stage (I) and the beginning of stage (II) are plotted in the range $0 < \varepsilon < 0.0025$. Stage (IV) starts at $\varepsilon = 0.1379$ for the pure iron and at $\varepsilon = 0.1503$ for the low-alloy steel. The yield stress values were determined for each material and deformation step according to [1], as the intersection of the pre-yield and post-yield branches in the Kocks-Mecking curves. The first characteristic to notice in Fig. 3 is that both materials exhibit in stages (I) and (II) upper and lower yield points followed by a yield plateau, which is associated

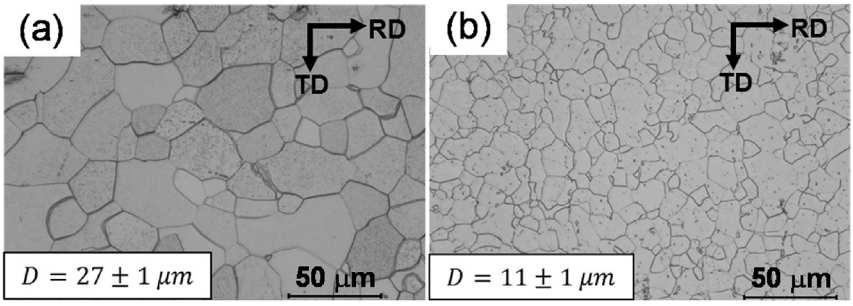

Fig. 2. Initial microstructures for the as-received (a) pure iron and (b) steel. The grain size, measured according to the equivalent diameter criterion, and principal directions are included in the figure.

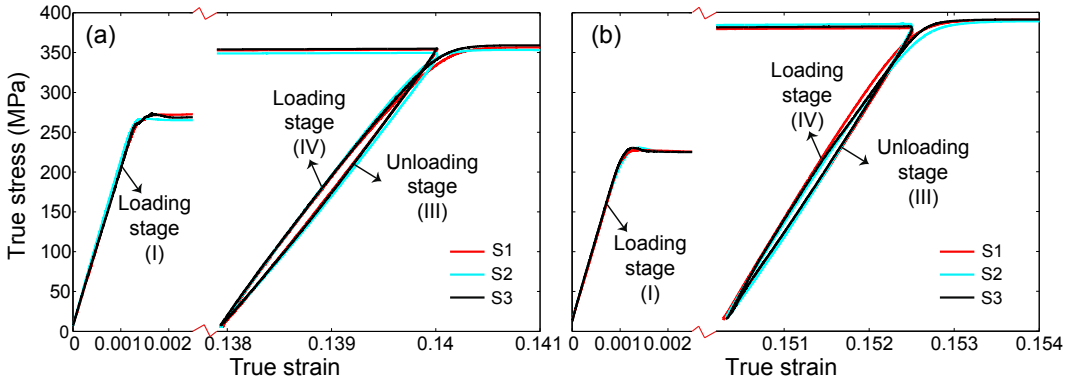

Fig. 3. True stress-true strain curves of the three tested specimens (S1, S2 and S3) for the (a) pure iron and (b) steel. The stages (II), (V) and (VI) are not shown.

with carbon solute atoms diffusing to dislocations. The macroscopic yield stress in stage (I), 265 MPa for the pure iron and 229 MPa for the low-alloy steel, respectively, will be reached after most of the dislocations break away from these solute atoms and Frank-Read sources are activated by the mechanism described in Section 2. Thus, the higher the solute carbon content of the material, the higher the yield stress: it is more difficult for the dislocations to leave these obstacles behind. Another important point, which is also observed in this stage, is that the steel exhibits a lower average yield stress than the pure iron (229 vs. 265 MPa). Besides the solute strengthening effect above mentioned, several other strengthening mechanisms, for example due to grain size, dislocations and precipitates, can contribute to the yield strength difference [14–16]. Since the carbon content of the pure iron is an order of magnitude smaller than that of the steel, its grain structure is significantly coarser (27 μm, see Fig. 2) and no precipitates are present, the larger yield stress of this material is most likely explained by a higher dislocation density. During plastic deformation in stage (II) and just before unloading, by contrast, the highest stress level is reached for the steel, which displays the greatest degree of work hardening. The average yield stress values in the second deformation step (stages IV and V) are 355 and 390 MPa, for the pure iron and the low-alloy steel, respectively. An additional feature can be observed in Fig. 3: the stress-strain hysteresis during unloading and re-loading. This hysteresis behaviour suggests that anelastic strain does occur and influences the pre-yield and unloading deformation behaviour [2,3], even for these two simple materials. The area of the hysteresis loop is the work dissipated by this anelastic strain.

In order to analyse the anelastic behaviour, the derivative of the stress-strain curves $\Theta_{pre} = d\sigma/d\varepsilon$ was calculated during loading in the pre-yield regime (for the stages (I) and (IV) in Fig. 3) and plotted in Fig. 4 as a function of the stress. This sort of plot is frequently found in the literature for the plastic regime of the materials and known as the Kocks-Mecking plot [10]. Since these plots aim to study the plastic behaviour, few of the ones presented in the literature include the stress range below the yield stress [1,17]. In the present work, the graph is untypically extended to zero stress and focusses on the pre-yield regime. For this reason, it will be referred to hereafter as the "extended" Kocks-Mecking plot [1]. In Fig. 4, the Θ_{pre} vs. σ data is plotted for the three tensile tests repeated for each material. It can be seen that even though small differences arise between specimens of the same material (red, blue and black curves), all curves display essentially the same shape, which can be well separated into two regions: in a first stage, the instantaneous modulus ($d\sigma/d\varepsilon$) of the material remains approximately constant (most clearly for the underformed materials, Fig. 4(a) and (c)) or it decreases slightly (for the deformed materials, Fig. 4(b) and (d)) whilst the stress increases. In a second stage, conversely, $d\sigma/d\varepsilon$ drops rapidly as the applied stress approaches the yield stress. It can also be noticed that the experimental data remains below the Young's modulus of the undistorted crystal lattice (210 GPa for both materials [18]), except for some points at the beginning of the curves in Fig. 4(a) and (c). It should be mentioned here that these Θ_{pre} values, which correspond to very small values of strain, are severely influenced by the derivation process which amplifies any noise present in the stress-strain curve.

Two key aspects can be extracted from the extended Kocks-Mecking plots: in this range of stresses the effective modulus is degraded relative to the Young's modulus and it is a non-linear function of the stress. In fact, near the yield stress the effective modulus decreases very quickly. As has been discussed in Section 2, this behaviour is due to limited dislocation glide by the bow-out mechanism, essentially without changes in the dislocation structure, and can be quantitatively described by Equation (9) (see Section 4.2).

It is interesting to note that when the curves of stages (I) and (IV) are compared (Fig. 4(a)-(b) for the pure iron and Fig. 4(c)-(d) for the steel), the latter always lie below the former. This means that the effective modulus degradation is larger on the previously deformed material during stage (IV). This is attributed to an increase in dislocation density due to the plastic strain applied during stage (II): the larger the plastic strain, the more dislocations contribute to the anelastic strain. As a result, the pre-yield modulus decreases from (I) to (IV). This variation of the effective modulus, dependent on prior plastic strain, has been reported in the literature [19,20]. In some cases, it has been observed that after the effective modulus decreased to certain extent, there was a saturation: successive deformation did not lead to further decrease [19]. Also, it is known that the effective modulus can be restored by recovery heat treatments [21]. So far, however, it has not been possible to accurately predict the modulus degradation after plastic strain.

4.2. Pre-yield model application

Consider the extended Kocks-Mecking plot of the pure iron in the first test (stage (I), Fig. 4(a)) and take the first specimen (S1, red curve) as an example. According to [1], the yield stress can be unambiguously determined as the transition point between the pre-yield and post-yield regimes (the latter is not included here, since this work focusses on the former), which have different slopes. This transition point is reached at the critical stress of $\sigma_c =$ 267 MPa for this sample. As pointed out before, an effective dislocation segment length can be calculated from this value and Equation (7), using $\overline{M} = 3.06$ [22], $G = 81$ GPa [18] and $b = 0.248$ nm, which results in $l = 233$ nm. It should be mentioned, however,

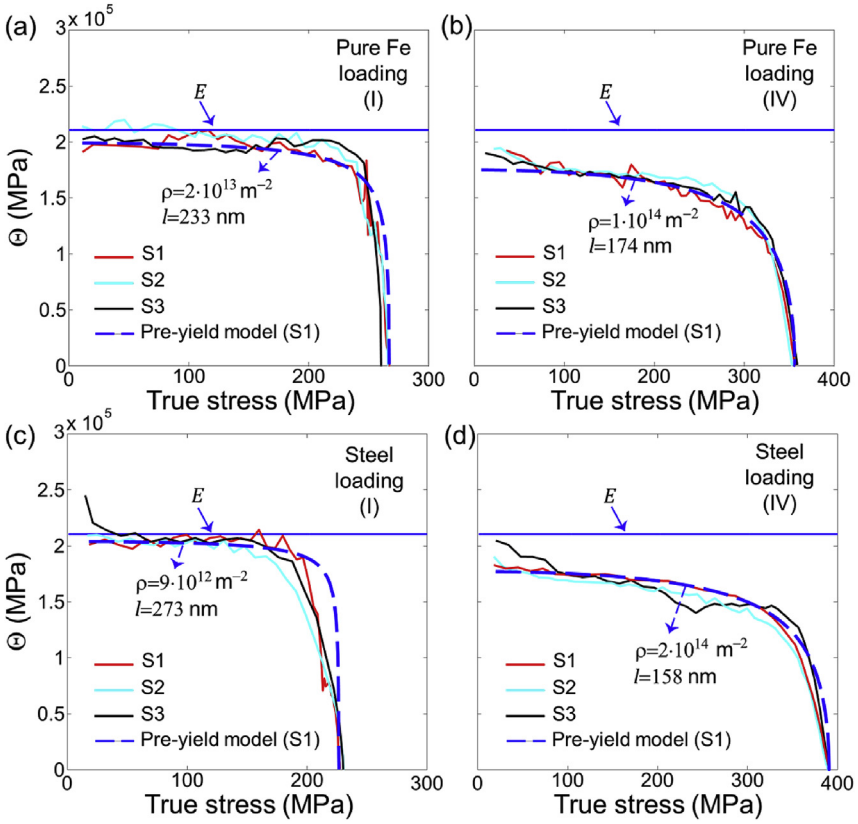

Fig. 4. Extended Kocks-Mecking plots obtained for the (a)–(b) pure iron and (c)–(d) steel in the pre-yield loading stages (I) and (IV), respectively. Values of the dislocation density ρ and effective dislocation segment length l obtained from pre-yield model analysis for sample S1 are included. Also, the theoretical Young's modulus E (210 GPa) is indicated.

that Equation (7) does not consider grain boundary effects and thereby the effective dislocation segment length could be somewhat underestimated. The initial value of the apparent Young's modulus or pre-yield stiffness of this sample, $\Theta_{pre}(\sigma \rightarrow 0)$, can be determined from the plot at small stress values. In this case, $\Theta_{pre}(\sigma \rightarrow 0) = 199$ GPa. Using now Equation (2), the initial anelastic contribution to the pre-yield deformation behaviour can be determined, $\Theta_a(\sigma \rightarrow 0) = 3636$ GPa. Once this value is known, the approximation $\varphi = l/r$, which is valid only for small stress values and simplifies Equation (8) to

$$\Theta_a = 3\overline{M}^2 E \Big/ \left[\rho l^2 (1+\nu)\right] \tag{10}$$

can be employed to calculate the initial dislocation density within the material [4]. Using $\nu = 0.29$ [19] and the previously derived value of l, Equation (10) leads to a dislocation density $\rho = 2{\cdot}10^{13}$ m^{-2}. Finally, substituting these values of ρ and l into Equation (9), the model curve corresponding to S1 (blue dashed line) in Fig. 4(a) results. As is seen here, the model is able to accurately reproduce the entire pre-yield deformation behaviour. It thus allows the characterisation of the two parameters reflecting the dislocation structure in the specimen. Note that ρ and l are calculated with relatively simple equations and the full curve follows from these values without additional fitting. Thus, simple mechanical tests can provide valuable insight into the dislocation structure and mechanisms occurring at the scale of dislocations.

This procedure was repeated for the other pure iron samples and those of the steel, using the extended Kocks-Mecking plots obtained in each case. The resulting model curves, for the stages (I) and (IV), corresponding to the first specimen analysed (S1), are included in Fig. 4. Excellent agreement between experimental data and model curves is observed in all cases. The values of ρ and l calculated for different specimens and averaged for the same stage and material (i.e., ρ_T and l_T) are summarised in Table 2, together with the standard deviations. The product ρl^2 is also included. Regarding the results in Table 2, the pure iron has, in the initial state, a higher dislocation density and a shorter segment length than the low-alloy steel, explaining why this material exhibits a higher yield stress than the steel in stage (I), in spite of its coarser grains. Due to plastic deformation (stage (II)), the dislocation density increases for both materials, diminishing the effective segment length: $\rho = 1{\cdot}10^{14}$ m^{-2} and $l = 174$ nm in the case of the pure iron and $\rho = 2{\cdot}10^{14}$ m^{-2} and $l = 158$ nm for the steel. Remarkably, the two materials present similar values for ρl^2 (with some small variations) in the as-received state and after plastic deformation. This ρl^2 product represents the dislocation structure (different combinations of dislocation densities and effective dislocation segment lengths) and is usually assumed to be $\rho l^2 \sim 1$ in the literature [4,23]. This is in excellent agreement with the ρl^2 values obtained for the as-received pure iron and steel in this work, that is, for relatively

Table 2
Average dislocation density (ρ_T) and effective segment length (l_T) calculated through the model detailed in Section 2. The dispersion in the measurements (SD) and the product $\rho_T l_T^2$ is also included.

Material	Condition	ρ_T (m^{-2})	SD (m^{-2})	l_T (nm)	SD (nm)	$\rho_T l_T^2$	SD
Pure Fe	As-received	$1.9{\cdot}10^{13}$	$6{\cdot}10^{12}$	235	2	1.0	0.3
	Deformed (14%)	$1.3{\cdot}10^{14}$	$1{\cdot}10^{13}$	174	1	4.0	0.3
Steel	As-received	$9.5{\cdot}10^{12}$	$1{\cdot}10^{12}$	270	2	0.7	0.1
	Deformed (15%)	$1.8{\cdot}10^{14}$	$2{\cdot}10^{13}$	158	1	4.5	0.5

simple dislocation structures. It is observed here, however, that the more complex the dislocation network (i.e., higher dislocation densities), the higher this product, as results for the plastically deformed pure iron and steel, for which $\rho l^2 \sim 4$. Therefore, the ρl^2 value can be considered as an indicative of the dislocation network complexity.

4.3. Reversibility of the anelastic strain

As seen in previous sections, the pre-yield deformation behaviour of the pure iron and the low-alloy steel can be accurately characterised by considering the elastic and anelastic contributions. The mechanism proposed in this work implies that below the yield stress, the limited dislocation glide (i.e., the bow-out mechanism) should in principle be reversible. In order to investigate the validity of this assumption, a loading-unloading cycle below the yield point was performed for the low-alloy steel after 3% plastic deformation (similar behaviour is expected for the pure iron). The aim of this experiment is to analyse the reversibility of the strain once dislocations can glide (dislocations are released from the C solute atoms when plastic deformation is applied), exemplifying stage (IV). The results corresponding to this experiment are plotted in Fig. 5(a) and Fig. 5(b), respectively, which illustrate the true stress-true strain cycle below the yield stress and subsequent Kocks-Mecking curves (Θ vs. σ curves). Fig. 5(a) confirms that the strain is largely reversible except for the small stress-strain hysteresis that is observed. The width of the loop at the end of unloading, which denotes the unrecoverable strain, i.e. microsplasticity, is $\varepsilon_{mp} = 6.2{\cdot}10^{-5}$, which is considerably smaller than the pre-yield strain, $\varepsilon_{pre} = 1.5{\cdot}10^{-3}$, and its anelastic component, $\varepsilon_a = 2.9{\cdot}10^{-4}$ (calculated as the difference in strain between a straight line with slope 210 GPa and the end of loading in the pre-yield regime). It is evident from Fig. 5(b) that Θ has similar values during loading and unloading, excluding the last part of the curves, in which the loading branch shows a larger degradation of Θ. Indeed, the initial values of Θ at loading are recovered at the beginning of unloading, which suggests that the dislocation structure remains essentially constant during the loading-unloading cycle: Frank-Read sources do not become operative in this stress region. The microplasticity seen in Fig. 5(a) is therefore not related to irreversible changes occurring in these dislocation structures.

The hysteresis behaviour observed in this experiment can be explained, as thoroughly detailed in Ref. [1], taking the obstacles within the microstructure into account. During unloading, these obstacles act opposite to the line tension of the dislocations and in the same direction as the applied stress. Therefore, only when the stress has decreased to certain extent, the dislocations will be able to pass these obstacles. This is the origin of the hysteresis that is observed here: the strain applied during loading is recovered during unloading, but at a lower stress level. It may occur, however, that some obstacles are not passed by the dislocations during unloading, explaining the differences observed in Fig. 5(b) at the end of loading and unloading, and some microplasticity occurs. It should be mentioned that this type of microplasticity, which is exhausted in the first cycle, occurs only during cyclic straining and is of no consequence for the events taking place during monotonous loading. It can therefore be concluded that the pre-yield deformation behaviour involves reversible glide of dislocations.

4.4. Dislocation densities determined by X-Ray Diffraction (XRD)

In order to assess the model validity, the dislocation density was also determined using XRD. The rather involved analysis of the XRD-peaks was proposed in Refs. [12,13] and is described in Appendix A. Fig. 6(a) shows, as an example, the diffraction patterns that were obtained for the as-received and plastically deformed steel, in which the peaks were fitted to Voigt functions. The profiles of the as-received materials were taken as a reference to remove instrumental broadening (see Appendix A), which implies that the calculated dislocation density, $\Delta\rho_{XRD}$, is the difference in dislocation densities derived from the deformed and as-received states. In the following paragraphs some crucial steps of the proposed method are discussed in detail.

The first step to determine the dislocation density is to calculate the dislocation contrast factor $\overline{C}$, which is given by Equation (A. 8). According to this equation, $\overline{C}$ depends on the parameter q, which indicates the character of the dislocations, the average contrast factor for the (h00) reflection $\overline{C}_{h00}$, and the constant $H^2 = (h^2k^2 + h^2l^2 + k^2l^2)/(h^2 + k^2 + l^2)^2$. The parameter q is determined from the $(\Delta K^2 - \alpha)/K^2$ vs. H^2 plot, illustrated in Fig. 6(b) for both materials, as the intercept of the regression line with the horizontal H^2 scale. Here, K is the scattering vector given by $K = 2\sin\theta/\lambda$, ΔK refers to the full width at half maximum and α is the inverse of the crystallite size. The value of $\overline{C}_{h00}$ is determined using ANIZC software [24], assuming the elastic constants of the iron and the steel as $C_{11} = 230.1$ GPa, $C_{12} = 134.6$ GPa and $C_{44} = 116.6$ GPa [25], and equal proportions of screw and edge dislocations. This results in an average $\overline{C}_{h00}$ value of 0.29. The experimental values of q are summarised in Table 3. All obtained q values are within the bounds specified by the theoretical values for edge and screw dislocations

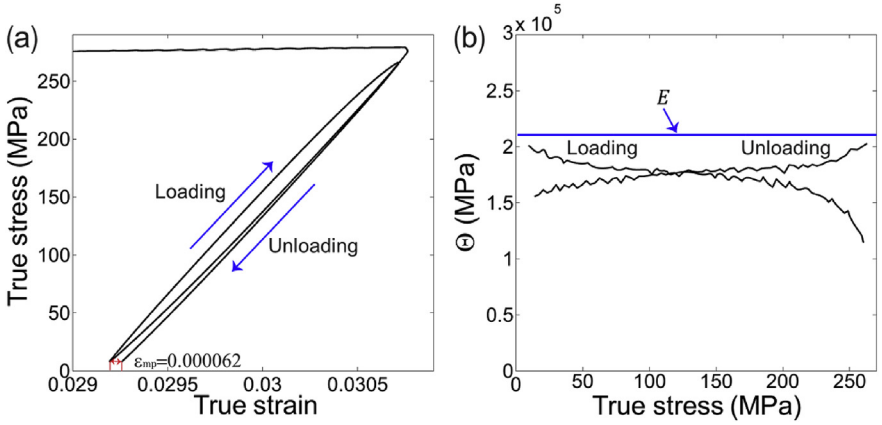

Fig. 5. Tensile test performed on the low-alloy steel to check the reversibility of strain in the pre-yield regime. (a) The loading-unloading cycle after 3% plastic strain and (b) its corresponding Kocks-Mecking curves.

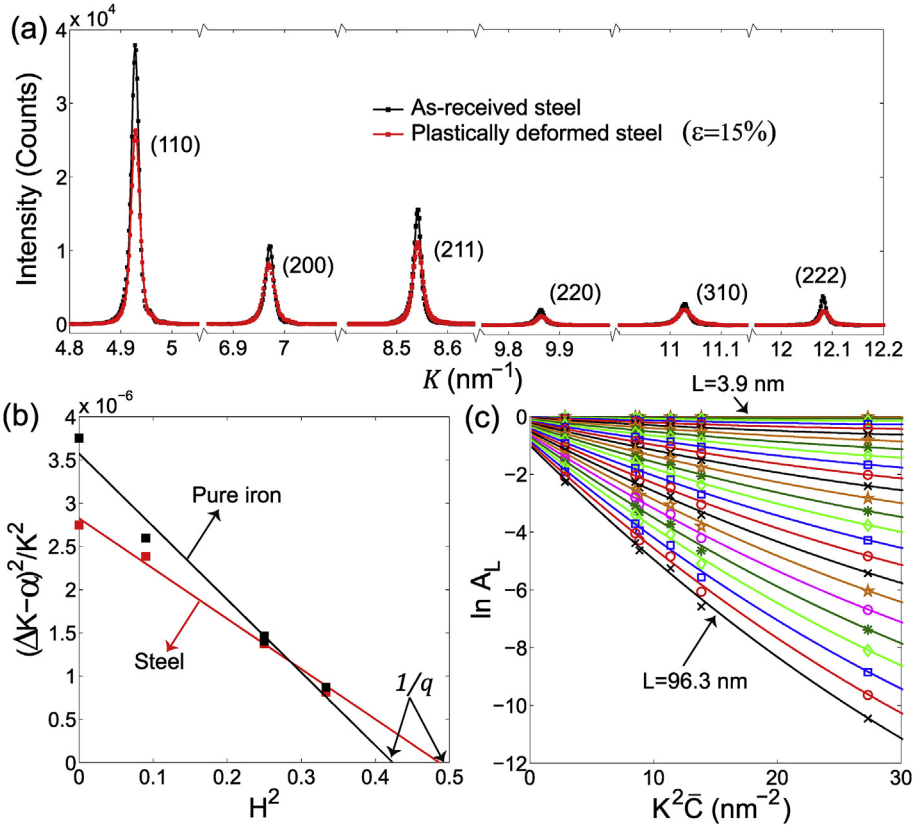

Fig. 6. (a) XRD diffraction patterns obtained for the steel in the as-received (taken as a reference) and plastically deformed (after stage III) conditions. The Miller indices are indicated in the figure. (b) Linear relationship between $(\Delta K^2 - \alpha)/K^2$ and H^2 in Equation (A. 10) for the pure iron and steel. (c) Example of the mWA plot obtained for the steel. Here, L values are taken in the range between $L = 3.9$ nm and $L = 96.3$ nm, with increments of $\Delta L = 3.9$ nm.

reported in Ref. [32] for iron, that is, 1.28 and 2.67, respectively.

For the modified Warren-Averbach analysis the Fourier transform of the diffraction peaks is considered. The real part of the Fourier coefficient A_L is determined by [26]:

$$A_L = \exp\left(- 2LF_L - \pi L^2 F_G^2 \right) \tag{11}$$

where L is the Fourier length and F_L and F_G are the Lorentzian and Gaussian components of the full width at half maximum, respectively (see Equations (A. 2)–(A. 6)). Fig. 6(c) displays, as an example, the mWA plot ($\ln A_L$ vs. $K^2\overline{C}$ for different L values) obtained for the steel. From the fitting of a second-order polynomial to the $\ln A_L$ vs. $K^2\overline{C}$ curves, $X(L)$ in Equation (A. 15) can be estimated. Dividing $X(L)$ by L^2 and plotting the result as a function of $\ln L$, Fig. 7 results. $\Delta\rho_{XRD}$ is determined from the slope of the regression line fitted to the $X(L)/L^2$ vs. $\ln L$ data points, for the linear part of the curve observed at small L values. The cut-off radius of dislocations R_e is then calculated from the intersection of that line with the vertical $X(L)/L^2$ axis. Finally, the parameter M, which indicates the arrangement between dislocations, can be determined as $M = R_e\sqrt{\Delta\rho_{XRD}}$. The $\Delta\rho_{XRD}$ and M values determined in this manner from Fig. 7 are summarised in Table 3, in which the larger dislocation density of the steel should be noticed for these specimens.

The average values of $\Delta\rho_{XRD}$, which are based on two measurements, are plotted in Fig. 8 together with the values calculated from the extended Kocks-Mecking curves for the tensile tests, $\Delta\rho_T$ (i.e., the difference in dislocation densities derived from the stages (IV) and (I)). The figure evidences the very good agreement between XRD and the pre-yield model. It is also noticed the higher accuracy of the latter approach, which is associated with the

Table 3
Experimental values of q, M and dislocation density ($\Delta\rho_{XRD}$) obtained by XRD for the specimens analysed in Figs. 6 and 7.

Material	q	$\Delta\rho_{XRD}$ (m^{-2})	M
Pure Fe	2.1	$1.6\bullet10^{14}$	1.2
Steel	2.4	$2.9\bullet10^{14}$	1.5

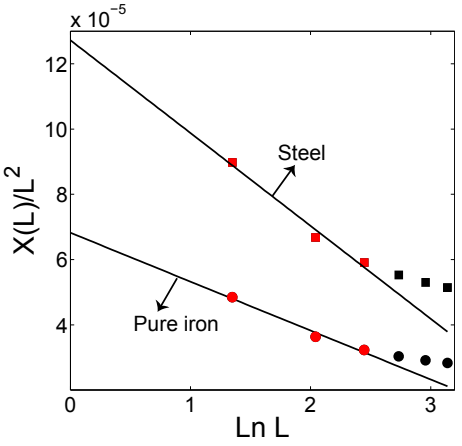

Fig. 7. $X(L)/L^2$ vs. $\ln L$ plot for the pure iron and steel. The straight line fitted to the linear part of the curve for small L values is also included. The points considered for the fitting are in red.

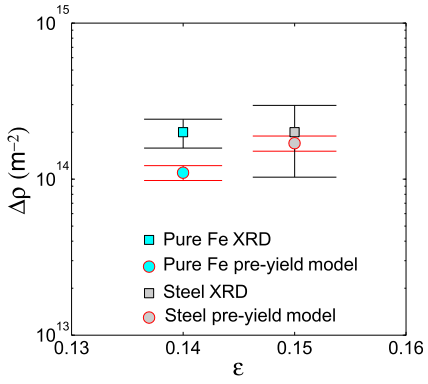

Fig. 8. Dislocation density values obtained by XRD ($\Delta\rho_{XRD}$), using the methodology explained in appendix A, compared with the dislocation density values calculated by application of the pre-yield model to the tensile curves ($\Delta\rho_T$).

smaller sensitivity of $\Delta\rho_T$, through the analysis method, for instrumental variations. An important conclusion can be drawn from this figure: the application of the pre-yield model to the tensile curves and the XRD analysis lead to similar values of dislocation density, which confirms the validity of the pre-yield model as a powerful and valuable tool to quantify dislocation structures.

5. Conclusions

The pre-yield deformation behaviour of pure iron and a low-alloy steel has been studied in the present work. It has been demonstrated that for these simple materials, in addition to linear elastic behaviour according to Hooke's law, anelastic strain does occur during loading in the pre-yield regime. A loading-unloading cycle below the yield stress, which has been performed for the low-alloy steel after 3% plastic deformation, has evidenced that deformation in this regime involves reversible glide of dislocations without changes in the dislocation structure. A physically-based model has been used to describe the pre-yield deformation behaviour and quantify the dislocation structures within the materials. The main conclusions of the study can be summarised as follows:

- The pre-yield model, based on two variables that characterise the dislocation structure, that is, the dislocation density and the effective dislocation segment length, accurately describes the pre-yield deformation behaviour of these materials.
- Applying the model to the extended Kocks-Mecking curves obtained by tensile tests, the dislocation structures within the pure iron and the steel have been characterised at different deformation conditions. The increase in dislocation density and the decrease of the segment length have been quantitatively determined.
- The dislocation density values obtained through the model have been confirmed by XRD, using the combination of the mWH and mWA approaches.

Acknowledgements

This research was supported by the Dutch Technology Foundation (STW) and carried out under the project number S22.1.13494b in the framework of the Research Program of the Materials innovation institute (M2i) (www.m2i.nl). The support of M2i and Tata Steel RD&T is gratefully acknowledged. The authors wish to thank Rob Delhez, Niek van de Pers and Ruud Hendrikx for the discussions on XRD analysis. The authors would also like to thank Ton Riemslag for his support in the mechanical tests.

Appendix A. X-Ray Diffraction (XRD) analysis

The methodology adopted in this work to determine the dislocation density from XRD profiles is based on a combination of the modified Williamson-Hall and modified Warren-Averbach methods [12,13]. The first approach is used to calculate the average contrast factor of dislocations $\overline{C}$, which is applied in the mWA method to determine the dislocation density. The procedure can be summarised as follows:

Voigt fitting and instrumental broadening. The XRD profiles were fitted to a Voigt function g_V (see Fig. 6(a) for the steel), which is the convolution of the Lorentzian g_L and Gaussian g_G functions:

$$g_V = g_G \otimes g_L \tag{A.1}$$

The fitting was done in reciprocal space (intensity vs. K) using the Levenberg-Marquardt algorithm. As input parameters, the initial estimates of the amplitude, position, Gaussian standard deviation (σ_G) and Lorentzian half width at half maximum (H_L) of the peaks were used. The full width at half maximum for the Gaussian (F_G), Lorentzian (F_L) and Voigt (F_V) functions were then calculated for the different materials as[27,28]:

$$F_G = 2\sqrt{2\ln 2}\sigma_G \tag{A.2}$$

$$F_L = 2H_L \tag{A.3}$$

$$F_V = 0.5346F_L + \sqrt{0.2166F_L^2 + F_L^2} \tag{A.4}$$

The instrumental broadening was subtracted using [29]:

$$(F_G^y)_p^2 = (F_G^y)_o^2 - \left(F_G^{ref}\right)^2 \tag{A.5}$$

$$(F_L^y)_p = (F_L^y)_o - \left(F_L^{ref}\right) \tag{A.6}$$

where the superscript y refers to the plastically deformed pure iron and steel, and the superscript *ref* denotes the reference material (i.e., the as-received pure iron and steel). Here, $(F_{G,L}^y)_p$ are the physical Gaussian and Lorentzian widths and $(F_{G,L}^y)_o$ the observed ones, respectively. Once the physical values of F_G^y and F_L^y are known, those of F_V^y are calculated by Equation (A. 4).

The modified Williamson-Hall (mWH) approach. Assuming that strain broadening is caused by dislocations only, the equation to describe the peak broadening is [12]:

$$\Delta K = (0.9/D) + \left(\pi M^2 b^2/2\right)^{1/2}\rho^{1/2}K\overline{C}^{1/2} + O\left(K^2\overline{C}\right) \tag{A.7}$$

in which K is the diffraction vector defined as $K = 2\sin\theta/\lambda$, where θ is the Bragg angle and λ is the wavelength of X-rays. In Equation (A. 7), ΔK is the full width at half maximum, D is the average crystal size, M is a constant depending on the effective outer cut-off radius of dislocations R_e and the dislocation density ρ, by $M = R_e\sqrt{\rho}$ [30], $\overline{C}$ is average contrast factor of dislocations and $O(K^2\overline{C})$ stands for higher order terms in $K\overline{C}^{1/2}$. Since the fitting of the XRD-peaks to a Voigt function was done in reciprocal space, $\Delta K = F_V^y$ in Equation (A. 7). In this equation, M is a dimensionless parameter which was first introduced by Wilkens and characterises the arrangement of dislocations [30]. The lower the value of M, the stronger the correlation between dislocations. For an untextured cubic polycrystalline material the average contrast factor of dislocations $\overline{C}$ can

be calculated using [31]:

$$\overline{C} = \overline{C}_{h00}\left(1 - qH^2\right) \tag{A.8}$$

in which $\overline{C}_{h00}$ is the average dislocation contrast factor for the (h00) reflection, q is a parameter that depends on the edge or screw character of dislocations and $H^2 = (h^2k^2 + h^2l^2 + k^2l^2)/(h^2 + k^2 + l^2)^2$. The value of $\overline{C}_{h00}$ and theoretical values of q, for either edge or screw dislocations, can be determined based on the elastic constants of the material and the active slip systems, and are therefore known values [12,32]. According to [12], the quadratic form of Equation (A. 7) can be approximated to:

$$\Delta K^2 \cong (0.9/D)^2 + \left(\pi M^2 b^2/2\right)\rho K^2 \overline{C} \tag{A.9}$$

where higher order terms in $K^2\overline{C}$ are neglected. Moving the size term to the left-hand side of the equation, dividing by K^2 and substituting Equation (A. 8) into Equation (A. 9), the following relation results:

$$\left(\Delta K^2 - \alpha\right)/K^2 = \left(\pi M^2 b^2/2\right)\rho \overline{C}_{h00}\left(1 - qH^2\right) \tag{A.10}$$

where $\alpha = (0.9/D)^2$. Applying this relation to ΔK values obtained for the different (hkl) reflections, the α parameter can be estimated from the $(\Delta K^2 - \alpha)/K^2$ versus H^2 plot, as the optimal value for linear regression. This is shown in Fig. 6(b) for both materials. Then, the experimental value of q can be determined as the intercept of that line with the horizontal H^2 axis.

The modified Warren-Averbach (mWA) approach. The Fourier transform of the X-ray profiles A_L can be obtained as the multiplication of the Fourier transforms of size and strain coefficients (A_L^S and A_L^D, respectively):

$$A_L = A_L^S \cdot A_L^D \tag{A.11}$$

The logarithm of the Fourier transform of the normalised intensity is expressed as [33]:

$$\ln A_L = \ln\left(A_L^S \cdot A_L^D\right) = \ln A_L^S - 2\pi^2 L^2 K^2 \left\langle \varepsilon^2 \right\rangle \tag{A.12}$$

where L is the Fourier length defined as $L{=}na_3$, in which n are integers, a_3 is the unit of the Fourier length in the direction of the diffraction vector K, given by $a_3 = \lambda/2(\sin\theta_2 - \sin\theta_1)$, and θ_1 and θ_2 are the starting and end values of the diffraction angular range in which each (hkl) peak is measured. $\langle\varepsilon^2\rangle$ is the mean squared strain caused by dislocations, which for small L values is approximated as [30,34]:

$$\left\langle \varepsilon^2 \right\rangle = \left(\rho \overline{C} b^2/4\pi\right)\ln(R_e/L) \tag{A.13}$$

Substituting Equation (A. 13) into Equation (A. 12) results in.

$$\ln A_L = \ln A_L^S - \rho\left(\pi b^2/2\right)L^2 \ln(R_e/L) K^2 \overline{C} \tag{A.14}$$

which is known as the mWA equation. Higher order terms in $K^2\overline{C}$ are considered negligible. In order to determine ρ, $\ln A_L$ as a function of $K^2\overline{C}$ is fitted by a second-order polynomial for given values of L (see Fig. 6(c) for the case of the steel). The coefficient of the cuadratic term, $X(L)$, is then given by

$$X(L)/L^2 = \rho\left(\pi b^2/2\right)(\ln R_e - \ln L) \tag{A.15}$$

Plotting the result as a function of $\ln L$, the slope of the straight line fitted to the data at low L, yields the dislocation density (see Fig. 7). R_e and M can be calculated from the intersection of that straight line with the vertical $X(L)/L^2$ axis and $M = R_e\sqrt{\rho}$, respectively.

References

[1] P. van Liempt, J. Sietsma, A physically based yield criterion I. Determination of the yield stress based on analysis of pre-yield dislocation behaviour, Mater. Sci. Eng. A 662 (2016) 80–87.
[2] R.M. Cleveland, A.K. Ghosh, Inelastic effects on springback in metals, Int. J. Plast. 18 (2002) 769–785.
[3] H. Kim, C. Kim, F. Barlat, E. Pavlina, M.G. Lee, Nonlinear elastic behaviors of low and high strength steels in unloading and reloading, Mater. Sci. Eng. A 562 (2013) 161–171.
[4] G. Schoeck, Dislocation theory of plasticity of metals, Adv. Appl. Mech. 4 (1956) 229–274.
[5] L. Sun, R.H. Wagoner, Complex unloading behaviour: nature of the deformation and its consistent representation, Int. J. Plast. 27 (2011) 1126–1144.
[6] Z. Chen, U. Gandhi, J. Lee, R.H. Wagoner, Variation and consistency of Young's modulus in steel, J. Mater. Proc. Technol. 227 (2016) 227–243.
[7] A.K. Ghosh, A physically-based constitutive model for metal deformation, Acta Metall. 28 (1980) 1443–1465.
[8] P.S. Alexopoulos, C.W. Cho, C.P. Hu, L. Che-Yu, Determination of the anelastic modulus for several metals, Acta Metall. 29 (1981) 569–577.
[9] D. Kuhlmann-Wilsdorf, Dynamic effects in the mesh length theory of work-hardening, Acta Metall. 37 (1989) 3217–3223.
[10] U.F. Kocks, H. Mecking, Physics and phenomenology of strain hardening: the FCC case, Prog. Mater. Sci. 48 (2003) 171–273.
[11] A. Krabiell, W. Dahl, Zum einfluss von Temperatur und Dehngeschwindigkeit auf die Streckgrenze von Baustählen unterschiedlicher Festigkeit, Arch. Eisenhüttenwes. 52 (1982) 429–436.
[12] T. Ungár, I. Dragomir, Á. Révész, A. Borbély, The contrast factors of dislocations in cubic crystals: the dislocation model of strain anisotropy in practice, J. Appl. Crystallogr. 32 (1999) 992–1002.
[13] T. Ungár, J. Gubicza, P. Hanák, I. Alexandrov, Densities and character of dislocations and size-distribution of subgrains in deformed metals by X-ray diffraction profile analysis, Mater. Sci. Eng. A 319–321 (2001) 274–278.
[14] F. HajyAkbary, J. Sietsma, A.J. Böttger, M.J. Santofimia, An improved X-ray diffraction analysis method to characterize the dislocation density in lath martensitic structures, Mat. Sci. Eng. A 639 (2015) 208–218.
[15] N. Isasti, D. Jorge-Badiola, M. Taheri, P. Uranga, Microstructural and precipitation characterization in Nb-Mo microalloyed steels: estimation of the contributions to the strength, Met. Mater. Int. 20 (2014) 807–817.
[16] J. Lu, O. Omotoso, J.B. Wiskel, D.G. Ivey, H. Henein, Strengthening mechanisms and their relative contributions to the yield strength of microalloyed steels, Metall. Mater. Trans. A 43 (2012) 3043–3061.
[17] M. Abspoel, B.M. Neelis, P. van Liempt, Constitutive behaviour under hot stamping conditions, J. Mat. Process. Technol. 228 (2016) 34–42.
[18] G. Ghosh, G.B. Olson, The isotropic shear modulus of multicomponent Fe-base solid solutions, Acta Mater. 50 (2002) 2655–2675.
[19] J.A. Benito, J.M. Manero, J. Jorba, A. Roca, Change of Young's modulus of cold-deformed pure iron in a tensile test, Metall. Mater. Trans. A 36 (2005) 3317–3324.
[20] R. Pérez, J.A. Benito, J.M. Prado, Study of the inelastic response of TRIP steels after plastic deformation, ISIJ Int. 45 (2005) 1925–1933.
[21] K. Yamaguchi, H. Adachi, N. Takakura, Effects of plastic strain and strain path on Young's modulus of sheet metals, Met. Mater. Int. 4 (1998) 420–425.
[22] R.E. Stoller, S.J. Zinkle, On the relationship between uniaxial yield strength and resolved shear stress in polycrystalline materials, J. Nucl. Mater. 283–287 (2000) 349–352.
[23] N.F. Mott, A theory of work-hardening of metal crystals, Philos. Mag. 43 (1952) 1151–1178.
[24] A. Borbély, J. Dragomir-Cernatescu, G. Ribárik, T. Ungár, Computer program ANIZC for the calculation of diffraction contrast factors of dislocations in elastically anisotropic cubic, hexagonal and trigonal crystals, J. Appl. Crystallogr. 36 (2003) 160–162.
[25] N. Armstrong, P. Lynch, Determining the dislocation contrast factor for X-ray line profile analysis, in: E.J. Mittemeijer, P. Scardi (Eds.), Diffraction Analysis of the Microstructure of Materials, vol. 68, Springer Series in Materials Science, 2004, pp. 249–286.
[26] D. Balzar, H. Ledbetter, Voigt-function modelling in Fourier analysis of size and strain broadened X-ray diffraction peaks, J. Appl. Crystallogr. 26 (1993) 97–103.
[27] N. Hagen, M. Kupinski, E.L. Dereniak, Gaussian profile estimation in one dimension, Appl. Opt. 46 (2007) 5374–5383.
[28] J.J. Olivero, R.L. Longbothum, Empirical fits to the Voigt line width: a brief review, J. Quant. Spectrosc. Radiat. Transf. 17 (1977) 233–236.
[29] Th.H. De Keijser, J.I. Langford, E.J. Mittemeijer, A.B.P. Vogels, Use of the Voigt function in a single line method for the analysis of X-ray diffraction line broadening, J. Appl. Crystallogr. 15 (1982) 308–314.
[30] M. Wilkens, Theoretical aspects of kinematical X-ray diffraction profiles from crystals containing dislocations distributions, in: J.A. Simmons, R. de Wit,

R. Bullough (Eds.), Fundamental Aspects of Dislocation Theory, vol. 2, National Bureau of Standards, Washington, DC, USA, 1970, pp. 1195–1221.
[31] T. Ungár, G. Tichy, The effect of dislocation contrast on X-ray line profile in untextured polycrystals, Phys. Status Solidi (a) 171 (1999) 425–434.
[32] J. Gubicza, X-ray Line Profile Analysis in Materials Science, USA: IGI-Global, Hershey, PA, 2014.
[33] B.E. Warren, X-ray studies of deformed metals, Prog. Met. Phys. 8 (1959) 147–202.
[34] M.A. Krivoglaz, Theory of X-ray and thermal neutron scattering by real crystals, Plenum Press, New York, 1969.